1 **Emergent dynamic chirality in a thermally driven artificial spin ratchet**

2 Sebastian Gliga[1,2,3,*], Gino Hrkac[4], Claire Donnelly[2,3], Jonathan Büchi[2], Armin

3 Kleibert[3], Jizhai Cui[2,3], Alan Farhan[2,3,5], Eugenie Kirk[2,3], Rajesh V. Chopdekar[6],

4 Yusuke Masaki[7], Nicholas S. Bingham[2,3,8], Andreas Scholl[5], Robert L. Stamps[1],

5 Laura J. Heyderman[2,3]

6 1 School of Physics and Astronomy, University of Glasgow, Glasgow, G12 8QQ, United Kingdom.

7 2 Laboratory for Mesoscopic Systems, Department of Materials, ETH Zurich, 8093 Zurich, Switzerland.

8 3 Paul Scherrer Institut, 5232 Villigen PSI, Switzerland.

9 4 College of Engineering, Mathematics and Physical Sciences, University of Exeter, Exeter, EX4 4QF,

10 United Kingdom.

11 5 Advanced Light Source, Lawrence Berkeley National Laboratory (LBNL), 1 Cyclotron Road, Berkeley,

12 California 94720, USA.

13 6 Department of Materials Science and Engineering, University of California, Davis, Davis, CA 95616,

14 USA.

15 7 Department of Physics, The University of Tokyo, Tokyo, 113-0033, Japan.

16 8 National Research Council Research Associate at the U.S. Naval Research Laboratory 4555 Overlook

17 Ave., SW Washington, DC 20375.

18 **Modern nanostructure fabrication techniques have opened the possibility to**

19 **create novel functional materials, whose properties transcend that of their**

20 **constituent elements. In particular, tuning the magnetostatic interactions in**

21 **geometrically-frustrated arrangements of nanoelements called artificial spin**

22 **ice[1,2] can lead to specific collective behaviour[3] including emergent magnetic**

23 **monopoles[4,5], charge screening[6,7] and transport[8,9] as well as magnonic**

24 **response[10-12]. Here, we demonstrate a spin-ice based active material in which**

25 **energy is converted into unidirectional dynamics. Using x-ray photoemission**

26 **electron microscopy we show that the collective rotation of the average**

27 **magnetisation proceeds in a unique sense during thermal relaxation. Our**

28 **simulations demonstrate that this emergent chiral behaviour is driven by the**

topology of the magnetostatic field at the edges of the nanomagnet array, resulting in an asymmetric energy landscape. In addition, a bias field can be used to modify the sense of rotation of the average magnetisation. This opens the possibility of implementing a magnetic Brownian ratchet[13-14], which may find applications in novel nanoscale devices, such as magnetic nanomotors, actuators, sensors or memory cells.

Chirality is a ubiquitous phenomenon in nature present in a variety of systems, from elementary particles, through the charge-parity violation of the weak interaction, to biomolecules whose function is defined by their handedness. In artificial systems, such as optical metamaterials, structural chirality can be exploited to control light-matter interactions and produce circularly polarized light[15]. In ferromagnets and antiferromagnets, the Dzyaloshinskii-Moriya interaction can give rise to chiral spin textures[16] and lead to non-reciprocal dynamics[17]. While most studied phenomena rely on a static view of chirality – *Is a system superimposable to its mirror image?* – this definition can be extended to include electric and magnetic fields as well as dynamic properties[18]. In this context, *dynamic* chirality applies to both chiral as well as achiral objects that display a preferred sense of rotation. In classical mechanics, an example is the rattleback: a spinning top that only rotates in one direction, while in chemistry, the interactions between an adsorbed molecule and a crystal surface can lead to the rotation of the molecule in a preferred direction[19].

Here we present an example of emergent dynamic chirality in an artificial spin ice system – a 'chiral ice'. Schematically represented in Fig. 1, the system consists of a two-dimensional arrangement of lithographically patterned single-domain nanomagnets in which the magnetisation points in one of two orientations along the magnet long axis due to shape anisotropy[1]. The choice of the array design is such that it is structurally chiral, *i.e.* it cannot be superimposed onto its mirror image, when considering the edges of the array. The two-dimensional character of the system is

56   constrained by the shape anisotropy of the nanomagnets (see Methods). Each vertex

57   is associated with four nanomagnets oriented at a 90° angle with respect to each

58   other and the net magnetisation is the sum of the individual magnetisation vectors of

59   the four elements within a vertex. We observe that, after applying and removing a

60   sufficiently large external field to saturate the array (see Methods), the thermally

61   activated relaxation at room temperature is characterized by the rotation of the net

62   magnetisation at individual vertices in a unique direction: from state A to state B, as

63   illustrated in Fig. 1. No statistically significant fraction of the vertices evolves from

64   state A to state D, thus defining a ratchet in which the magnetostatic energy supplied

65   by the saturating field is transformed into the clockwise rotation of the average

66   magnetisation. This is a realisation of active matter: an out of equilibrium system that

67   locally converts energy into directed motion[20,21]. In the presence of a small bias field,

68   heating allows the vertices to evolve into state C (Fig 1, array with dark contrast). In

69   thermal equilibrium, a preferred direction of rotation does not occur due to

70   microscopic reversibility. Chiral evolution is however possible if the system is far from

71   equilibrium and in the presence of an asymmetric potential[22]. Using micromagnetic

72   simulations, we find that an asymmetry is indeed generated in our system as a result

73   of the topology of the stray field of the nanomagnet array. At the edges of the array,

74   the stray field gives rise to emergent patterns, whose specific rearrangement during

75   the thermal evolution can decrease the energy of the system, reminiscent of the role

76   of magnetic surface charges in a ferromagnet. It is the energy decrease that

77   accompanies the reordering of these 'emergent charges' that drives the chiral

78   dynamics of the system during the thermal relaxation.
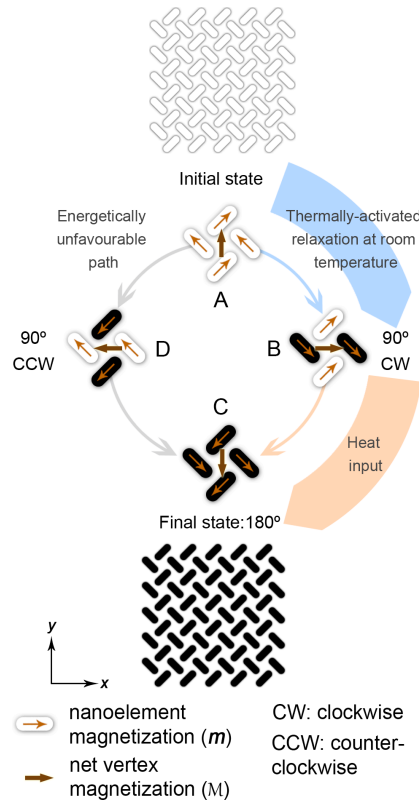
Fig. 1: Schematic representation of the chiral ice and evolution of the net magnetization at individual vertices within the array. The thermally activated evolution after initial saturation along the +y direction (state A) is shown, with the white or black colour, respectively indicating the direction of the magnetisation m toward the positive or negative y axis. The thin orange arrows represent the magnetization within the nanoelements while the net magnetisation at each individual vertex, M, is indicated by the large brown arrows at the centre of the vertices. The thermal relaxation at room temperature takes place stepwise via a clockwise (CW) rotation of the net magnetisation by 90° to state B and is indicated by the blue arrows. When the system is heated above room temperature in the presence of a bias field, the average magnetisation can locally rotate further (orange arrows), to state C. Considering the evolution from state A, state D statistically occurs with very low probability. The net vertex magnetisation therefore consistently rotates clockwise.

The experimental system consists of a finite array of elongated Permalloy nanomagnets arranged on a square grid as illustrated in Fig. 2a. An image of the full array is shown in Supplementary Information S1. We use soft x-ray photoemission electron microscopy (PEEM) exploiting x-ray magnetic circular dichroism (XMCD) to image the magnetic state of the individual nanomagnets. In the XMCD images (Fig. 2b), the nanomagnets in which the magnetisation is parallel to the direction of the x-rays display a bright contrast, whereas nanomagnets in which the magnetisation is

98   reversed display a dark contrast. The homogeneous XMCD contrast for each

99   nanomagnet confirms that they are in a single-domain state. The nanomagnets are

100   sufficiently thin (see Methods), such that thermal energy can overcome the energy

101   barrier to switch between the two possible single domain states at room temperature.

102   The thickness is chosen so that the switching rates are comparable to the PEEM

103   measurement time scale[23,24]. We first apply a saturating magnetic field, H_{sat} (see

104   Methods), such that, after its removal, the average remanent magnetisation of the

105   array points along the positive y direction (Fig. 2c, where all nanomagnets display a

106   bright contrast). The measured time evolution of the magnetisation over a period of

107   21 hours is shown in Fig. 2d-h in the presence of a weak bias field, as indicated in

108   Fig. 2 (see Methods). The formation of regions with 'checkerboard' magnetic contrast

109   pattern observed in Fig. 2d indicates that the average magnetisation at these vertices

110   has evolved from state A to state B (see also Fig. 2b for a detailed view of state B),

111   and have hence rotated by 90° in the clockwise (CW) direction. The evolution slows

112   down considerably after ca. 4 hours, indicating that the system approaches thermal

113   equilibrium, as explained in Supplementary Information S2. Heating the sample by a

114   few Kelvin ensures that the thermal evolution, and therefore the rotation of vertices

115   from state A to B, continues while vertices already in state B evolve into state C (dark

116   contrast regions in Fig. 2e where the net magnetisation has locally rotated by 180°).

117   Throughout the evolution, the rotation of the net vertex magnetisation M (see Fig. 2b)

118   starts at the edges of the array and propagates towards its centre. The heat-assisted

119   rotation continues until the magnetisation in the array has mostly rotated by 180° with

120   respect to state A (Fig. 2h). The quantitative evolution of the different vertex types (A,

121   B and C) as well as the heating schedule are shown in Supplementary Information

122   S3.

123   To confirm that the observed chiral behaviour is a magnetostatically-driven effect, we

124   performed similar measurements on systems with a larger relative distance between

125 nanomagnets, in which the strength of the magnetostatic interaction was reduced,

126 and found that the thermal evolution became achiral (see Supplementary Information

127 S4). We also note that we did not observe any preferred direction of rotation in

128 structures consisting of a single vertex with four nanomagnets, despite their structural

129 chirality. A chiral structure by itself is therefore not sufficient to generate the observed

130 dynamics: in the following we show that the dynamics is driven by the existence of an

131 emergent asymmetric magnetostatic energy landscape.

132
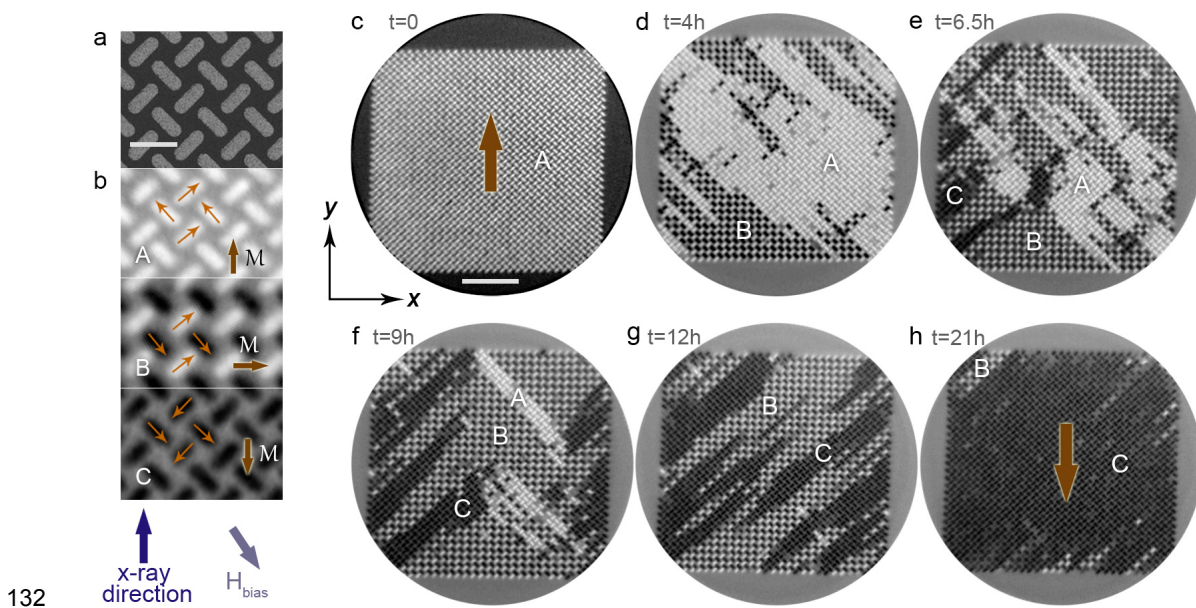
Fig. 2: Measured clockwise evolution of the magnetisation following saturation along the +y direction. (a) Top: Scanning electron microscopy (SEM) image of a region of the investigated array. The scale bar represents 600 nm. (b) XMCD contrast for states A, B and C, with arrows showing the orientation of the magnetisation for selected nanomagnets and the net vertex magnetisation in each case, indicated with a larger brown arrow and denoted M. (c) XMCD image of the array following saturation along the +y direction. The vertices are in state A with the average magnetisation within the array indicated by the large brown arrow. The detailed magnetic configuration of state A is shown in (b). The scalebar represents 5 µm and the field of view is of 25 µm. The contrast was adjusted for better visibility. (d-h) Time evolution of the magnetisation in the presence of a bias field. The magnitude of H_{bias} is between 50 µT and 80 µT, in the indicated direction. In (d), thermal relaxation at room temperature gives rise to domains of vertices in state B, mainly nucleating from the array edges and whose detailed magnetic configuration is shown in (b). The sample temperature was subsequently increased by a few Kelvin for four hours to ensure that the magnetisation reversals continue, as seen in (e-g). In (e), domains of vertices in state C [shown in panel (b)] nucleate from the edges of the array. Around t = 15 hours, the sample was heated again to achieve a close-to-complete 180° reversal of the magnetisation, observed in (h).

6

149   We performed micromagnetic simulations to qualitatively understand why the

150   clockwise evolution of the magnetisation is favoured over the counterclockwise

151   evolution. The simulated system is a finite system identical to the one shown in Fig.

152   1, with the same geometry as the experimentally studied one, but with fewer magnets

153   due to the computational cost of simulating the entire experimental array (see

154   Methods). We consider the system without the bias field in order to determine its

155   intrinsic thermal behaviour. Fig. 3a is a close-up of a section of the simulated array,

156   following saturation and removal of the field H_{sat} (equivalent to state A in Fig. 2)**.** The

157   magnetostatic volume charges, $\rho = -\boldsymbol{\nabla} \cdot \boldsymbol{M}$, are plotted inside the nanomagnets

158   along with the generated stray field outside the nanomagnets. The stray field displays

159   a complex topology owing to the presence of antivortex patterns. Antivortices are

160   two-dimensional structures characterised by a field distribution in which the direction

161   of the field revolves clockwise around a central point[25] as schematically illustrated in

162   the inset of Fig. 3a, where the centre of the structure is indicated with an orange dot.

163   Because antivortices typically occur inside ferromagnets, we refer to the observed

164   stray field patterns as *virtual* antivortices, *i.e.* whose centre is located outside the

165   nanomagnets[26]. Such virtual structures have previously been reported to play a role

166   in the stability of magnetisation patterns[25] as well as in the dynamics of coupled

167   systems[27]. Considering the entire simulated array (Fig. 3b), the distribution of the

168   virtual antivortices within the system following saturation is plotted in Fig. 3c. The

169   overall stray field topology effectively forms a virtual antivortex crystal, in which the

170   antivortices, represented by orange dots, display an ordered arrangement within the

171   bulk of the array. At the edges, the distribution of the virtual antivortices breaks the

172   symmetry of the bulk arrangement. Moreover, the distribution of the virtual

173   antivortices is different when comparing the horizontal edges (top and bottom;

174   highlighted in blue) with the vertical edges (left and right; highlighted in red). The

175   virtual antivortex distribution for a partial clockwise rotation of the vertex

176   magnetisation by 90° (state B) along four diagonals of the array is given in Fig 3d.

177 This corresponds to the magnetic state labelled 'CW 1' in Fig. 3f where the four

178 diagonals can be seen and which is representative of experimentally observed

179 configurations. Within the bulk of the simulated array, the arrangement of the virtual

180 antivortices is modified: in domains where the net vertex magnetisation has rotated

181 by 90° (dark grey regions), the antivortex stray field patterns are also rotated by 90°.

182 At the edges of such domains (light grey regions), the antivortices are rotated by 45°,

183 mirroring the rotation of the average magnetisation of those vertices. It is, however,

184 along the array edges that the most significant changes take place: while the number

185 of virtual antivortices remains constant, they have been rearranged compared to Fig.

186 3c. This is analogous to the situation in a finite-sized ferromagnet, where the stray

187 field energy can be minimised through the rearrangement of surface charges,

188 $\sigma = \boldsymbol{M} \cdot \boldsymbol{n}$ (where $\boldsymbol{n}$ is a normal vector to the surface), and result in the formation of

189 domains within the ferromagnet. The rearrangement of the virtual antivortices in

190 alternating patterns along the array edges is thus reminiscent of the pole avoidance

191 principle in ferromagnets, which leads to the minimization of the magnetostatic

192 energy through a reduction of the total magnetic charge. In the studied system the

193 virtual antivortices thus function as emergent surface charges whose rearrangement,

194 through the rotation of the magnetisation, minimises the total energy of the system

195 during relaxation. In Fig. 3e, the emergent charge distribution is given for a system

196 with four diagonals along which the average magnetisation has rotated

197 counterclockwise. This distribution corresponds to the magnetic state labelled 'CCW

198 1' in Fig. 3f, where the vertices along those diagonals are in state D (see Fig. 1).

199 When compared to Fig. 3d, the overall virtual antivortex structure is generally

200 mirrored (along an axis defined by the saturation direction, *y*), except at the edges,

201 where their distribution is not mirrored. Our simulations show that these differences

202 lead to an asymmetric energy landscape in which the energy of the system

203 decreases more efficiently through the clockwise (CW) rotation of the net vertex

204 magnetisation at the edges than through the counterclockwise (CCW) rotation. We

8

plot in Fig. 3f the relative difference in energy barriers at 300 K between the initial

state (Fig. 3c) and the states in Figs. 3d and e, which are labelled as 'CW 1' and

'CCW 1'. The energy barrier to access the clockwise state is lower, thus making it

more probable. The energy barriers are also plotted for configurations in which

nanomagnets at the edges of the array have not switched. We find that, in these

cases, the energy barriers for the clockwise and counterclockwise rotations of the net

vertex magnetisation become equal. These results demonstrate that the chiral

behaviour is driven by the edges of the system and that the observed initial clockwise

rotation of the net vertex magnetisation following saturation is due to the intrinsically

asymmetric energy landscape of the system.
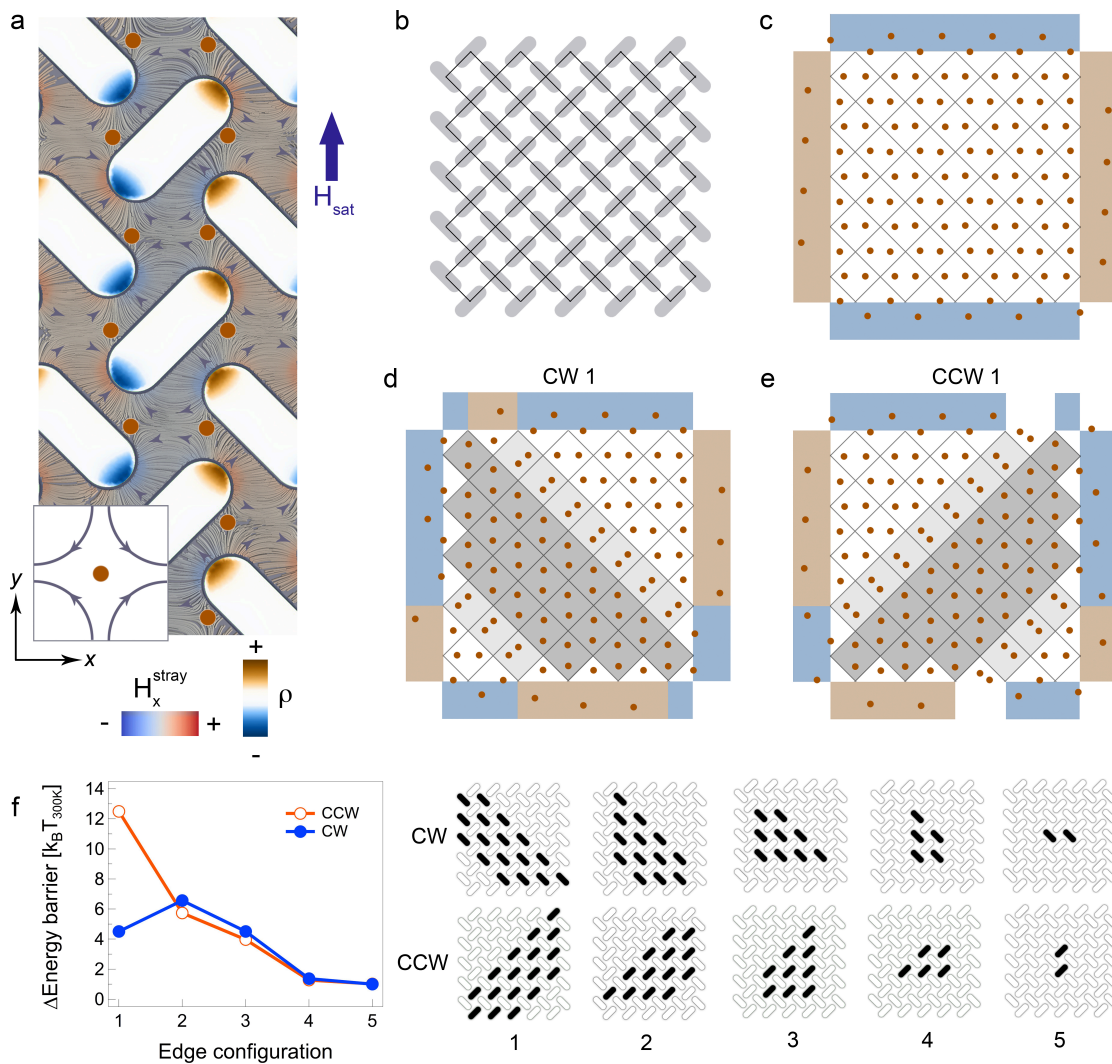
216 **Fig. 3: Simulated stray field structure and energy barriers for clockwise and counterclockwise**
217 **rotations of the average magnetisation.** (a) Stray field configuration for a portion of the simulated
218 nanomagnet array in state A, following saturation with the field H_{sat}. The centres of the virtual
219 antivortices are highlighted by orange dots and the magnetic volume charges (ρ) within the single-
220 domain nanomagnets are plotted using the blue-brown colormap. The x component of the stray field,
221 H_x^{stray}, is indicated by the blue-red colormap. An antivortex structure is schematically shown in the
222 bottom inset. (b) Wire frame representation of the array lattice. (c) Distribution of the virtual antivortices
223 (orange dots) in the array in state A, following saturation along the $+y$ direction. The different antivortex
224 distributions along the array edges are highlighted in red and blue. In (d), the virtual antivortex
225 distribution is plotted for a configuration in which the average magnetisation along four diagonals (dark
226 grey regions) was rotated clockwise by 90° (state B). The corresponding magnetic state of the array is
227 given in (f): configuration 'CW 1'. (e) Virtual antivortex distribution for a configuration in which the net
228 vertex magnetisation along four diagonals is rotated counterclockwise by 90°, corresponding to the
229 magnetic state 'CCW 1' in (f). In the white regions along the array edges in (e), the stray field distribution
230 is identical to the one in the bulk. (f) Relative energy barriers, starting from the remanent state (a), for
231 the shown configurations 1 – 5 in which the reversal of the magnetisation in edge nanoelements is
232 gradually set back. The black nanomagnets have switched, using the same colour convention, as in Fig.
233 1. The energies are normalized to configuration 5, where the barriers for the CW and CCW rotations of
234 the net vertex magnetisation are identical.

235 The evolution of the average magnetisation during relaxation at room temperature

236 eventually leads to thermal equilibrium. The measured continuous clockwise

237 evolution of the magnetisation in the experiment towards state C is thus enabled by

238 the bias field, which effectively modifies the energy landscape, such that the system

239 can access state C upon moderate heating. We have also found that the bias field

240 can, in some cases, be used to reverse the dynamic chirality. Indeed, by saturating a

241 system with identical geometry to the one in Fig. 2 (see Methods) in the opposite

242 direction (along the $-y$ direction, Fig. 4a) we observe that in the presence of H_{bias} the

243 relaxation can proceed through the counterclockwise rotation of the net vertex

244 magnetisation (Fig. 4b-d). It is thus in principle possible to use a bias field to enhance

245 the 'built-in' clockwise rotation or to favour the counterclockwise sense of rotation of

246 the average magnetisation by exploiting the asymmetric magnetostatic potential

247 generated by the edges.
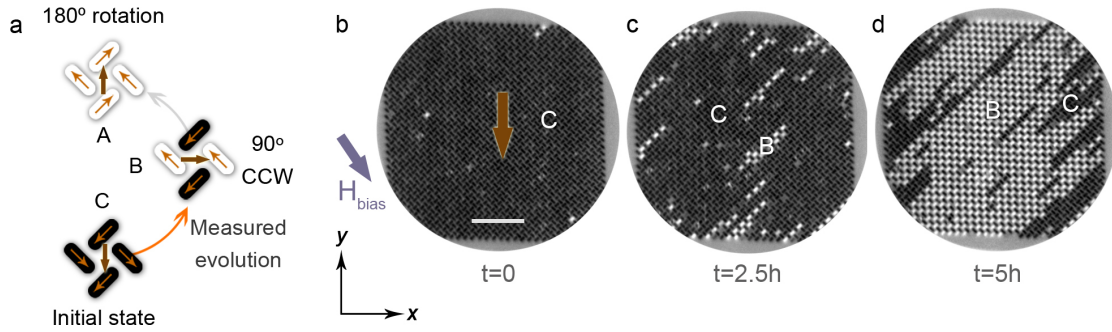
Fig. 4: Counterclockwise evolution of the system following saturation in the –*y* direction. (a) When the array is saturated along the –*y* direction, the magnetisation evolves counterclockwise, *i.e.* from state C to state B (orange arrow), in the presence of the bias field H_{bias}. (b-d) Measured time-evolution of the magnetisation. In (b), the array is in state C after saturation and the average magnetisation is indicated by the large brown arrow. The evolution towards the sate shown in (c) occurs at room temperature. Heating the sample for 2.5 hours allows accessing the state shown in (d). The rotation from state B to state A was not observed owing to the orientation of the bias field. We note that the counterclockwise rotation from state C to state B is observed in about 20% of the measured samples. Indeed, starting from state C, the counterclockwise evolution favoured by the bias field competes with the natural clockwise evolution of the system and can cause the array to remain, on average, in state C. The scalebar represents 5 μm.

The magnetostatic interaction offers a known route for symmetry breaking in ferromagnets that can lead to rich behaviour, such as surface and curvature-induced non-reciprocal spin wave[28,29] and domain wall[30,31] propagation. In contrast, in the studied artificial spin system the origin of the thermally activated unidirectional rotation of the average magnetisation is due to the dynamic rearrangement of emergent magnetic charges, which result from the geometry of the array edges. This introduces the possibility of exploiting artificial spin ices with tailored edge geometry and field-tunable dynamics as functional, active materials within devices that convert heat into motion, such as mesoscopic motors[20,22] or rotors[32]. It is also conceivable to include such a spin ratchet within hybrid multistacks, found for example in MRAM, in which the chiral array would form the active layer and the thermally activated rotation of the magnetisation in the array (triggered for example by means of laser pulses) could lead to a change in resistance across the stack without requiring a phase change material[33].

11

Methods

Sample Fabrication

Finite arrays of Permalloy ($Ni_{83}Fe_{17}$) nanomagnets were prepared on a silicon (100) substrate using electron beam lithography in conjunction with thermal evaporation at room temperature and a base pressure of 2×10^{-7} mbar followed by lift-off. The evaporation resulted in a nanocrystalline Permalloy film, which was capped by a 3 nm aluminium layer to protect against oxidation. The Permalloy film was evaporated with a thickness gradient along the sample in order to ensure the presence of a thermally active region at room temperature adequate for the PEEM measurements[24]. Array thicknesses were measured using Atomic Force Microscopy (AFM). The thermally active arrays in Fig. 2 and 4 had identical geometries and were manufactured from nanomagnets with length and width of 470 nm and 170 nm, and with a lattice constant of 425 nm (centre-to-centre distance of neighbouring nanomagnets: see Supplementary Information S1). The measured thickness of the arrays was: 2.2 nm in Fig.1 and 2.7 nm in Fig. 4. The thicknesses were uniform across each array. The magnetisation in both arrays rotated clockwise when saturated along the +y direction, demonstrating that the thickness variation between the arrays did not affect the sense of rotation of the magnetisation. The array in Supplementary Information S3 had a thickness of 2.4 nm. The chiral structure of the system is defined by the geometry of the array edges as well as by its two-dimensional character due to the shape anisotropy induced by the low Permalloy thickness, which ensures that the magnetisation is confined to the plane of the sample.

Experiment

299 Magnetic imaging was carried out with the photoemission electron microscopy

300 endstation[34] at the Surface/Interface: Microscopy (SIM) beamline of the Swiss Light

301 Source, Paul Scherrer Institute and at the PEEM-3 photoemission electron

302 microscope at beamline 11.0.1 of the Advanced Light Source, Berkeley National

303 Laboratory. Employing XMCD, the system was imaged by tuning the x-ray energy to

304 the Fe L_3-edge. The magnetic contrast images were obtained by pixelwise division of

305 two consecutive images recorded with right and left circular polarizations. The

306 resulting contrast is proportional to $\boldsymbol{k} \cdot \boldsymbol{m}$, where $\boldsymbol{k}$ is the propagation vector of the x-

307 rays and $\boldsymbol{m}$ the local magnetisation vector[35]. The sample orientation was optimized to

308 maximize the contrast. The uniform contrast within the nanomagnets indicates that

309 they were in a single-domain state. Nanomagnets with grey contrast were switching

310 faster than the measurement time. For observations of the magnetisation reversal at

311 the Swiss Light Source, the samples were mounted on a copper (nonmagnetic)

312 holder that allowed radiative heating of the sample and the temperature was

313 measured using a PT100 sensor placed close to the sample. During the experiments

314 the sample was exposed to a small constant bias field (H_{bias}) with an estimated in-

315 plane magnitude of 50 – 80 µT based on Hall probe measurements. The arrays were

316 saturated *in-situ* using a permanent magnet inserted into the PEEM chamber. The

317 saturating field strength at the location of the sample was of H_{sat}=15 mT in the plane

318 of the sample. The magnet was retracted from the chamber after saturation.

319 Measurements at the Advanced Light Source were carried out by saturating the

320 sample both *ex-situ* as well as in a holder with a built-in electromagnet, which

321 allowed us to apply fields up to 20 mT.

322 **Micromagnetic simulations**

323 Fully three-dimensional micromagnetic simulations based on a hybrid finite-

324 element/boundary-element method[36,37] have been carried out on a system of 60

325 nanomagnets, each with lateral dimensions 235 nm × 85 nm (50% of experimental

326 size) and 2 nm thick. The structure was discretized using a tetrahedral mesh with an

327 average edge length of 1 nm. The material parameters for Permalloy were: saturation

328 polarization $\mu_0 M_S$ = 1 T, exchange constant A = 1.3 × 10^{-11} J/m and zero

329 magnetocrystalline anisotropy K = 0 J/m^3. The total Gibbs magnetic free energy is

330 given by:

$$E(\boldsymbol{m}) = \int \left(A \left[\sum_{k}^{x,y,z} (\nabla m_k)^2 \right] + K[1 - (\boldsymbol{m} \cdot \boldsymbol{a})^2] - \frac{1}{2} \mu_0 M_S (\boldsymbol{H}_{\text{dem}} \cdot \boldsymbol{m}) \right.$$

$$\left. - \mu_0 M_S (\boldsymbol{H}_{\text{ext}} \cdot \boldsymbol{m}) \right) dV.$$

331 *E* is the sum of the exchange energy, the anisotropy energy, the demagnetising

332 energy, and the Zeeman energy. $\boldsymbol{m} = \boldsymbol{M}/M_S$ is the reduced magnetisation, *A* is the

333 exchange constant, *K* the magnetocrystalline anisotropy, *a* is a unit vector along the

334 magnetocrystalline anisotropy direction, $\boldsymbol{H}_{\text{dem}}$ is the demagnetising field and $\boldsymbol{H}_{\text{ext}}$ an

335 external field. The integral is over the magnetic volume. In the performed simulations

336 H_{ext}=0.

337 To understand the thermal stability and transition probability from the remanent state,

338 following the application of a saturating field, to different magnetic states, *i.e.*

339 configurations resulting from clockwise and counterclockwise rotations, we used the

340 nudged elastic band method to find the lowest possible energy transition path

341 between the two states[38]. We start from a magnetisation state, $\boldsymbol{M}_1$, where the

342 magnetic system occupies a local minimum. Through thermal activation, the system

343 can overcome the local energy barrier and move towards a different minimum state,

344 $\boldsymbol{M}_2$, following either clockwise or counterclockwise rotation of the vertex

345 magnetisation. The difference between the local minima and the saddle point in the

346 energy path gives the energy barrier that has to be overcome to move to the next

347 local minima; this determines the stability of the magnetic state. An optimization

algorithm is applied until, at any point along the path, the gradient of the energy is only pointing along the path. This represents the path with the greatest statistical weight. The state with the lowest energy barrier has the highest probability of being reached.

Data availability

The data that support the findings of this study are available from the corresponding author S.G. upon reasonable request.

Contributions

RLS and SG conceived the spin ice geometry and the experiment. SG, AF, CD and JC prepared the samples. SG, CD, JC, JB, AK, AF, RC, EK, AS, and NB performed the experiments and analysed the experimental data. GH, SG and JB performed and evaluated the micromagnetic simulations. SG, RLS, GH, JB, CD, AK, YM and LJH interpreted the results. SG wrote the manuscript with input from all coauthors. All authors discussed the results and commented on the manuscript.

Acknowledgements

References

1.   Wang, R. F. *et al.* Artificial 'spin ice' in a geometrically frustrated lattice of nanoscale ferromagnetic islands. *Nature* **439,** 303–306 (2006).

2.   Heyderman, L. J. & Stamps, R. L. Artificial ferroic systems: novel functionality from structure, interactions and dynamics. *Journal of Physics: Condensed Matter* **25,** 363201 (2013).

3.   Morrison, M. J., Nelson, T. R. & Nisoli, C. Unhappy vertices in artificial spin ice: new degeneracies from vertex frustration. *New Journal of Physics* **15,** 045009 (2013).

4.   Mengotti, E. *et al.* Real-space observation of emergent magnetic monopoles and associated Dirac strings in artificial kagome spin ice. *Nature Physics* **7,** 68–74 (2010).

5.   Vedmedenko, E. Y. Dynamics of Bound Monopoles in Artificial Spin Ice: How to Store Energy in Dirac Strings. *Physical Review Letters* **116,** 077202 (2016).

6.   Gilbert I, *et al.* Emergent ice rule and magnetic charge screening from vertex frustration in artificial spin ice. *Nature Physics* **10,** 670 (2014).

7.   Farhan, A. *et al.* Thermodynamics of emergent magnetic charge screening in artificial spin ice. *Nature Communications* **7,** 12635 (2016).

399   8.   Branford, W. R., Ladak, S., Read, D. E., Zeissler, K. & Cohen, L. F.

400   Emerging Chirality in Artificial Spin Ice. *Science* **335,** 1597–1600 (2012).

401   9.   Le, B. *et al.* Understanding magnetotransport signatures in networks of

402   connected permalloy nanowires. *Physical Review B* **95**, 060405(R)

403   (2017).

404   10.   Gliga, S., Kákay, A., Hertel, R. & Heinonen, O. G. Spectral Analysis of

405   Topological Defects in an Artificial Spin-Ice Lattice. *Physical Review*

406   *Letters* **110,** 117205 (2013).

407   11.   Jungfleisch, M. B. et al. Dynamic response of an artificial square spin

408   ice. *Physical Review B* **93**, 100401(R) (2016).

409   12.   Bhat, V. S, Heimbach, F., Stasinopoulos, I. and Grundler D.

410   Magnetization dynamics of topological defects and the spin solid in a

411   kagome artificial spin ice. *Phys. Rev. B* **93**, 140401(R) (2016).

412   13.   Kelly, T. R., De Silva, H. & Silva, R. A. Unidirectional rotary motion in a

413   molecular system. *Nature* **401**, 150–152 (1999).

414   14.   Mochizuki, M. *et al*. Thermally driven ratchet motion of a skyrmion

415   microcrystal and topological magnon Hall effect. *Nature Materials* **13**,

416   241 (2014).

417   15.   Gansel, J. K. et al. Gold helix photonic metamaterial as broadband

418   circular polarizer. *Science* 325, 1513–1515 (2009).

419   16.   Bode, M. *et al.* Chiral magnetic order at surfaces driven by inversion

420   asymmetry. *Nature* **447**, 190–193 (2007).

421   17.   Zakeri, Kh. *et al*. Asymmetric Spin-Wave Dispersion on Fe(110): Direct

422   Evidence of the Dzyaloshinskii-Moriya Interaction. *Physical Review*

423   *Letters* **104**, 137203 (2010).

424   18.   Barron, L. D. TRUE AND FALSE CHIRALITY AND PARITY VIOLATION.

425   *Chemical Physics Letters* **123,** 423–427 (1986).

426   19.   Hel-Or, Y., Peleg, S. & Avnir, D. Two-Dimensional Rotational Dynamic

427   Chirality and a Chirality Scale. *Langmuir* **6,** 1691–1695 (1990).

428   20.   Browne, W. R. & Feringa, B. L. Making molecular machines work. *Nature*

429   *Nanotechnology* **1,** 25–35 (2006).

430   21.   Romanczuk, P., Chaté, H., Chen, L., Ngo, S. & Toner, J. Emergent

431   smectic order in simple active particle models. *New Journal of Physics*

432   **18,** 063015 (2016).

433   22.   Hänggi, P. & Marchesoni, F. Artificial Brownian motors: Controlling

434   transport on the nanoscale. *Reviews of Modern Physics* **81**, 387–442

435   (2009).

436   23.   Kapaklis, V. et al. Thermal fluctuations in artificial spin ice. *Nature*

437   *Nanotechnology* **9**, 514–519 (2014).

438   24.   Farhan, A. *et al.* Exploring hyper-cubic energy landscapes in thermally

439   active finite artificial spin-ice systems. *Nature Physics* **9,** 1–8 (2013).

440   25   Gliga, S., Hertel, R. & Schneider, C. M. Switching a magnetic antivortex

441   core with ultrashort field pulses. *Journal of Applied Physics* **103,** 07B115

442   (2008).

443   26.   Dotse, D. & Arrott, A. A.. Micromagnetic studies of vortices leaving and

444   entering square nanoboxes. *Journal of Applied Physics* **97**, 10E307

445   (2005).

446   27.   Kumar, D., Barman, S. & Barman, A. Magnetic Vortex Based Transistor

447   Operations. *Sci. Rep.* **4,** 4180 (2014).

448   28.   Camley, R. E. Nonreciprocal surface waves. *Surface Science Reports* **7,**

449   103–187 (1987).

450   29.   Otálora, J. A., Yan, M., Schultheiss, H., Hertel, R. & Kákay, A.

451   Curvature-Induced Asymmetric Spin-Wave Dispersion. *Physical Review*

452   *Letters* **117,** 227203 (2016).

453   30.   Yan, M., Andreas, C., Kákay, A., Garcia-Sanchez, F. & Hertel, R. Chiral

454   symmetry breaking and pair-creation mediated Walker breakdown in

455   magnetic nanotubes. *Applied Physics Letters* **100,** 252401 (2012).

456   31.   Hertel, R. CURVATURE-INDUCED MAGNETOCHIRALITY. *SPIN* **03,**

457   1340009 (2013).

458   32.   Fletcher, S. P., Dumur, F., Pollard, M. M. & Feringa, B. L. A Reversible,

459   Unidirectional Molecular Rotary Motor Driven by Chemical Energy.

460   *Science* **310,** 80–82 (2005).

461   33.   Wong, H.-S. P. & Salahuddin, S. Memory leads the way to better

462   computing. *Nature Nanotechnology* **10**, 191 (2015).

463   34.   Le Guyader, L. *et al*. Studying nanomagnets and magnetic

464   heterostructures with X-ray PEEM at the Swiss Light Source. Journal of

465   Electron Spectroscopy and Related Phenomena **185**, 371-380 (2012).

466   35.   Stöhr, J. *et al.* Element-Specific Magnetic Microscopy with Circularly

467   Polarized X-rays. *Science* **259,** 658–661 (1993).

468   36.   Chantrell, R. W., Fidler, J., Schrefl, T., & Wongsam, M. Micromagnetics:

469   Finite Element Approach, in *Encyclopedia of Materials: Science and*

470   *Technology* p. 5651-5660 (Elsevier, 2001).

471   37.   Hertel, R. Guided Spin Waves, in *Handbook of Magnetism and*

472   *Advanced Magnetic Materials*. (John Wiley & Sons, 2007).

473   38.   Dittrich, R. *et al.* A path method for finding energy barriers and minimum

474   energy paths in complex micromagnetic systems. *Journal of Magnetism*

475   *and Magnetic Materials* **250,** L12 (2002).